White Rose Research Online

eprints@whiterose.ac.uk
https://eprints.whiterose.ac.uk
Universities of Leeds, Sheffield and York

Deposited via The University of Sheffield.

White Rose Research Online URL for this paper:
https://eprints.whiterose.ac.uk/id/eprint/247339/

Version: Published Version

Article:
Dubart, M., Druett, M., Ruan, W. et al. (2026) Beam-driven evaporation in 2.5D flare simulations with an asymmetric magnetic field configuration. The Astrophysical Journal, 1011 (1). 10. ISSN: 0004-637X

https://doi.org/10.3847/1538-4357/aea418

Reuse
This article is distributed under the terms of the Creative Commons Attribution (CC BY) licence. This licence allows you to distribute, remix, tweak, and build upon the work, even commercially, as long as you credit the authors for the original work. More information and the full terms of the licence here: https://creativecommons.org/licenses/

Takedown
If you consider content in White Rose Research Online to be in breach of UK law, please notify us by emailing eprints@whiterose.ac.uk including the URL of the record and the reason for the withdrawal request.

UNIVERSITY OF LEEDS
University of Sheffield
UNIVERSITY of York

The Astrophysical Journal, 1011:10 (13pp), 2026 November 1 https://doi.org/10.3847/1538-4357/aea418
© 2026. The Author(s). Published by the American Astronomical Society.
OPEN ACCESS

Beam-driven Evaporation in 2.5D Flare Simulations with an Asymmetric Magnetic Field Configuration

M. Dubart[1], M. Druett[2], W. Ruan[3], and R. Keppens[1]
[1] Center for mathematical Plasma Astrophysics, Department of Mathematics, KU Leuven, Celestijnenlaan 200B, B-3001 Leuven, Belgium; maxime.dubart@kuleuven.be
[2] Plasma Dynamics Group, School of Electrical and Electronic Engineering, University of Sheffield, Sheffield, S1 3JD, UK
[3] Max-Planck Institute for Solar System Research, 37077, Göttingen, Germany
Received 2026 March 24; revised 2026 July 29; accepted 2026 September 2; published 2026 October 21

Abstract

The standard flare model is often depicted and studied starting from a perfectly antisymmetric magnetic field configuration with left−right symmetry in magnitude, on either side of the polarity inversion line. However, flare observations confirm that most flares have a significantly asymmetric magnetic field across the inversion line. To study asymmetric flare evolutions in both thermal and nonthermal components, self-consistent multidimensional models must incorporate nonlocal, beam-driven feedback on the stratified, thermal plasma. Here we present the first multidimensional magnetohydrodynamic flare simulation featuring evaporation driven by energetic electron beams that has an asymmetric background magnetic field configuration. The entire flare evolution depends significantly on those electron beams as they drive the evaporated plasma upward from the lower atmosphere. We study the impact of an asymmetric configuration on the evolution and geometry of a self-consistent, beam-driven flare loop system using the `MPI-AMRVAC` toolkit. We contrast the typical left−right symmetric case with the more realistic asymmetric setup. We observe the formation of a rotating flux rope, as well as an asymmetric behavior in the strength of hard X-ray (HXR) fluxes, and discuss the influence on the chromospheric evaporation at either footpoint. In line with the latest observational findings, our models display distinct spatiotemporal variation in the HXR emission and flare ribbon evolutions. In particular, we discuss how our model exhibits both the Sakao effect, where local field strength would anticorrelate with HXR source strengths, and the anti-Sakao effect, where local field strength would correlate with HXR source strengths, in the same simulation.

Unified Astronomy Thesaurus concepts: Solar physics (1476); Solar flares (1496); Magnetohydrodynamical simulations (1966); Magnetohydrodynamics (1964); Solar chromosphere (1479)

Materials only available in the online version of record: animation

1. Introduction

In recent works (W. Ruan et al. 2020; M. K. Druett et al. 2023; M. Druett et al. 2024), we introduced and parametrically investigated the first self-consistent flare simulations performed in multidimensional magnetohydrodynamical (MHD) settings, where nonthermal electron beams are coevolved with the thermal, fully stratified plasma. In analogy with many authors (e.g., P. F. Chen et al. 1999; I. Izquierdo-Guzmán et al. 2023), these models exploit an MHD setting, including a gravitationally stratified chromosphere, up to the corona. It features an initial vertical current sheet, and anomalously triggered resistivity that adapts to a more kinetic, current-based resistivity prescription and regulates the reconnection according to the standard flare scenario. Novel in the W. Ruan et al. (2020), M. K. Druett et al. (2023), and M. Druett et al. (2024) approach is that the thermal plasma evolution is augmented with field-aligned electron beams that deposit the energy they received through sub-grid-scale, parameterized acceleration at reconnection sites to the lower atmosphere. Since such beam prescriptions form essential ingredients of many state-of-the-art 1D hydrodynamic flare models (J. C. Allred et al. 2015; M. Carlsson et al. 2023), we can directly compare the impact of truly multidimensional effects on evaporation flows, soft X-ray (SXR) and hard X-ray (HXR) signals, and particle trapping.

The typical standard flare cartoon is usually drawn in a 2D cross section showing a left−right (a)symmetry. MHD-only 2D, 2.5D, and 3D evolutions (X. Kong et al. 2019; C. Shen et al. 2022; W. Ruan et al. 2023, 2024) eventually develop asymmetric features at those regions where the reconnection flows meet up with the flare loops underneath, or in the flare loop tops (F. Bacchini et al. 2024; C. Mora et al. 2026), due to a combination of MHD processes and instabilities. However, the initial stages retain a large degree of symmetry, especially during the rapid impulsive phase. Here we study an idealized generalization of the standard flare model that builds in a frequently observed initial asymmetry from the start of the flare onset.

Variations in the behaviors of flare energy release at different locations and times within a flare ribbon (V. Polito et al. 2023; G. S. Kerr et al. 2024b; A. G. M. Pietrow et al. 2024a), or in opposite-polarity footpoints and apparently magnetically connected flare footpoints (P. J. A. Simões et al. 2024; G. S. Kerr et al. 2026), have been highlighted by recent research as an outstanding opportunity to understand flare processes and evolution. Our current understanding is likely to increase via the latest international fleet of solar instrumentation: IRIS (B. De Pontieu et al. 2014), DKIST (T. R. Rimmele et al. 2020), and SPICE on board Solar Orbiter

Original content from this work may be used under the terms of the Creative Commons Attribution 4.0 licence. Any further distribution of this work must maintain attribution to the author(s) and the title of the work, journal citation and DOI.

(D. Müller et al. 2020; SPICE Consortium et al. 2020). Examples of this include the following:

1. The energy transport mechanisms that take energy from the corona to the flare ribbons, where different spectral signatures can be compared with modeling and theory (A. F. Kowalski et al. 2015; M. Druett et al. 2017; A. F. Kowalski et al. 2022; G. S. Kerr et al. 2024a). These have also enabled explorations of the timings and dynamics of energy delivery in footpoints on opposite ribbons at subsecond cadence (P. J. A. Simões et al. 2024).
2. Evidence of radiative back-warming has been obtained, where energy initially deposited in the atmosphere is further transported, including to deeper depths via radiative transport. This has been evidenced through theory and corroborated through observations of initial kernels of flare footpoint emission, with more diffuse halos highlighting the radiative back-warming in lines such as H_2 molecular emission (S. M. Mulay & L. Fletcher 2021; S. M. Mulay et al. 2023).
3. Inferences on the solar atmospheric evolution and their impacts on line profiles are providing further tools to assess the physics responsible for the latest observations of flare ribbon formation and substructures (M. Druett et al. 2017; G. S. Kerr et al. 2024b; A. G. M. Pietrow et al. 2024a; R. J. French et al. 2025; V. Singh et al. 2026; J. Thoen Faber et al. 2026).
4. Detailed understanding of the formation processes and dynamics around chromospheric/compressive downflows (A. F. Kowalski et al. 2015; V. Polito et al. 2023; G. S. Kerr et al. 2024a; A. G. M. Pietrow et al. 2024a) and hot ablative upflows into the corona (M. K. Druett et al. 2023; V. Polito et al. 2023).
5. Multidimensional flare energy transport via compression from nearby field lines and multidimensional radiative transfer (RT) computations (C. M. J. Osborne & L. Fletcher 2022; M. Druett et al. 2024).

Regarding the asymmetry of HXR sources at opposite footpoints of coronal loops, they have been observed to differ in intensity and spectral index, and the footpoint that has weaker magnetic field strength tends to have stronger HXR sources (T. Sakao 1994; T. Sakao et al. 1996). This field strength relationship has been termed "the Sakao effect." The Sakao effect was interpreted via magnetic mirroring of the energetic particles. That is, the converging magnetic field on the side with the stronger footpoint magnetic field stops a greater fraction of precipitating particles and their energy fluxes from reaching the lower atmosphere. P. Saint-Hilaire et al. (2008) noted that these asymmetries also tended to peak at the peak of the HXR flux, and they corroborated the Sakao effect using 172 observations of flare HXR taken with the Reuven Ramaty High Energy Solar Spectroscopic Imager (RHESSI; G. J. Hurford et al. 2002). However, it has also been noted that acceleration source symmetry was assumed to reach the interpretation of magnetic mirroring (P. Saint-Hilaire et al. 2008). Further, studies have also highlighted that the Sakao effect is not universal, with around one-third of flare footpoints showing higher HXR fluxes in the footpoints with the stronger field (C. P. Goff et al. 2004). This has been interpreted via atmospheric asymmetries, and such instances are sometimes termed as "non-Sakao" or N-type asymmetries (C. P. Goff et al. 2004; R. Falewicz & M. Siarkowski 2007). M. Jin & M. D. Ding (2007) also noted that the slower varying components of HXR sources are generally well correlated in opposite footpoints, but individual bursts are less correlated. They concluded that although small elementary injections of electron beams can be considered as essentially independent in each footpoint, the total integrated flux retains a high correlation. In a recent study, G. S. Kerr et al. (2026) showed that asymmetries in sets of flare ribbon footpoints can be interpreted as resulting from differing dominant energy transport mechanisms—with one footpoint response being driven by electron precipitation and the other (weaker HXR) footpoint being mainly driven by thermal heat flux.

X. Kong et al. (2019) and W. Ruan et al. (2020) propose mechanisms for the generation of HXR in coronal loop tops due to the trapping of energetic particles. X. Kong et al. (2019) suggest that the observed HXR in the loop top is a result of fast electrons being accelerated during the reconnection process by the termination shock, transported, and then trapped at the top of the flare loop, below the shock. This leads to small but strong HXR sources in the loop top. W. Ruan et al. (2020), in opposition, show weak but large HXR sources in the loop top, resulting from electrons being accelerated in the reconnection current sheet and then trapped in a larger region surrounding the termination shock. W. Ruan et al. (2020) showed that this trapping is directly related to the initial pitch-angle distribution of the electron beams that are injected at the reconnection acceleration sites. In a 3D MHD simulation of an erupting flux rope, H. Wu et al. (2025) showed that "mini flux ropes" with opposite helicity are responsible for different trajectories regarding the acceleration of electrons along the magnetic field lines, leading to double electron sources, in contrast to what is obtained in single X-point reconnection observed in 2D and 2.5D simulations. H. Wu et al. (2025) used test particle treatments injected in the fragmented current sheet that forms under the erupting flux rope.

Since many of these phenomena can be impacted by asymmetries in the flare loop system, our new asymmetric multidimensional flare simulations are a valuable tool to add critical information to the developing field of understanding flare substructure, ribbon formation, and evolution. Specifically, in this study we will test the impact that asymmetry of field strength and geometry can have on the responses in connected field line footpoints. This provides a crucial check for attributing observed behaviors to, e.g., different energy transport mechanisms and subsequent flare ribbon dynamics. Therefore, we will compare our symmetric and asymmetric flare simulations and investigate the following science question: using solely asymmetries in two-ribbon flare loop geometry, what degree of impact on behaviors can be accounted for regarding

1. the timings of flare ribbon formation onset and energy transport (G. S. Kerr et al. 2024b; P. J. A. Simões et al. 2024);
2. downflow variations at given plasma temperatures (M. K. Druett et al. 2023; M. Druett et al. 2024; G. S. Kerr et al. 2024b); and
3. evaporation fluxes (M. K. Druett et al. 2023; V. Polito et al. 2023; G. S. Kerr et al. 2024b).

Our paper is organized as follows: Section 2 introduces the numerical setup. Section 3 compares symmetric with asymmetric evolutions using beam-incorporated MHD descriptions, where we discuss both SXR and HXR flux evolutions and

perform detailed field line analysis for comparisons to the usual 1D flare model approach. Section 4 summarizes and concludes our findings.

2. Numerical Setup

We initialize our setup using the open-source MPI-parallelized Adaptive Mesh Refinement Versatile Advection Code (R. Keppens et al. 2012; O. Porth et al. 2014; C. Xia et al. 2018; R. Keppens et al. 2023). The governing magnetohydrodynamic equations are identical to W. Ruan et al. (2020) and M. K. Druett et al. (2023, 2024), and they include background heating (described by Equation (5) in W. Ruan et al. 2020), nonlocal field-aligned electron beam energy transport, gravitational stratification, resistivity, field-aligned thermal conduction, and optically thin radiative losses (J. Colgan et al. 2008). The latter ingredients allow us in principle to get thermal-instability-driven post-flare coronal rain condensations (W. Ruan et al. 2024; R. Keppens et al. 2025) or radiatively driven modifications to slow-mode wave behavior for straight thin flux tubes (S. Kumar et al. 2016; V. M. Nakariakov et al. 2017), but in the current simulations we do not find pronounced roles for thermal misbalance effects. The spatial domain extends from $X = -50$ Mm to $X = 50$ Mm and from $Y = 0$ Mm to $Y = 100$ Mm. The initial resolution of the simulation is 64 × 64 cells, which is equivalent to a grid separation of 1.5625 Mm. Thanks to adaptive mesh refinement (AMR), a resolution of 2048 × 2048 cells is achieved, equivalent to the finest grid separation of 48.8 km. This refinement is performed through six levels, with maximal refinement imposed below $y = 3$ Mm, and the cells that contain the dynamically integrated magnetic field lines. Automatic refinement is ensured via a weighting of 1:2:2 between mass density, vertical magnetic field, and energy density. We note that, despite the spatial domain being described in two dimensions, all vector quantities in this simulation are described in three dimensions. We refer to this type of simulation as 2.5D.

We employ a three-step time-stepping scheme and the Harten −Lax−van Leer (HLL) approximate Riemann solver (A. Harten et al. 1983) for the flux scheme. Similar to W. Ruan et al. (2020) and M. K. Druett et al. (2023, 2024), we use a combination of a third-order limiter (M. Čada & M. Torrilhon 2009), for regions of low refinement, and a second-order limiter (B. van Leer 1974), for regions of high refinement.

The VAL-C temperature profile is used as the initial temperature profile below the transition region height of $h = 2.543$ Mm (J. E. Vernazza et al. 1981). Above this height, the temperature profile is given by Equation (9) in W. Ruan et al. (2020). The number density at the lower boundary is given by $\rho = 4.6 \times 10^{14}$ cm^{-3}. The initial density is calculated based on hydrostatic equilibrium. Similarly to M. Druett et al. (2024), the side boundary conditions are treated as open. Parameters ρ, p and $\boldsymbol{B}$ are fixed at the bottom boundary, and asymmetric conditions are employed for the velocity, in order to produce tied magnetic field lines. At the top boundary, an asymmetric condition is assigned to B_x, and the temperature is set according to $dT/dy = 0$ when the instantaneous local temperature $T_b < 5$ MK.

The anomalous resistivity method used to model chromospheric evaporation by electron beams is identical to M. Druett et al. (2024). The x-component of the magnetic field is

$$B_x = 0. \tag{1}$$

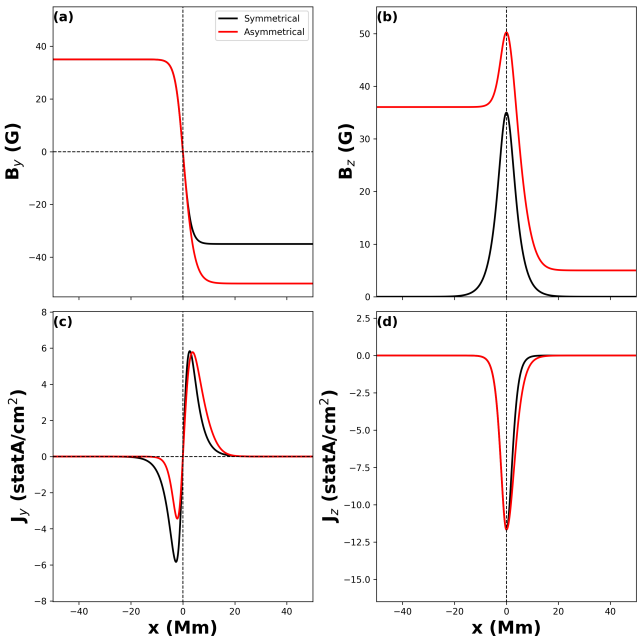


Figure 1. Magnetic field and current density y- and z-components for Equation (2) (in black, symmetric) and Equations (3) and 7 (in red, asymmetric). Panels (a) and (b) display the y- and z-components of the magnetic field, respectively, while panels (c) and (d) display the y- and z-components of the current density, respectively.

In W. Ruan et al. (2020) and M. K. Druett et al. (2023), the y- and z-components of the magnetic field were initialized as

$$\begin{aligned} B_y(x) &= -B_0 \tanh(x/w), \\ B_z(x) &= B_0/\cosh(x/w), \end{aligned} \tag{2}$$

where $B_0 = 35$ G and $w = 1.5$ Mm is the width of the current sheet. This results in a purely symmetric magnetic field configuration. In this study, we modified the initial magnetic field configuration compared to W. Ruan et al. (2020) to

$$B_y(x) = \begin{cases} -B_{\max} \tanh\left(\dfrac{x}{aB_{\max}}\right) & \text{for } x \geqslant 0, \\ -B_0 \tanh\left(\dfrac{x}{aB_0}\right) & \text{for } x < 0, \end{cases} \tag{3}$$

where $B_0 = 35$ G (left-side background field strength), $B_{\max} = 50$ G (right-side background field strength), and $a = 0.086$ Mm G^{-1} is a constant chosen such that $aB_0 = 3.0$ Mm. This constant a is introduced to mimic a current sheet width of $w = 3.0$ Mm, in a similar manner to that in W. Ruan et al. (2020). The relationship $B_{\max} = c_{\text{asy}} B_0$ is introduced to allow the magnetic field configuration to be asymmetric in the case where $c_{\text{asy}} \neq 1$. In our simulation, $c_{\text{asy}} = 1.4$ is a constant that has been chosen to produce a pronounced but not extreme amount of asymmetry. Panel (a) of Figure 1 shows the $B_y(x)$ component of the magnetic field for the symmetric configuration (in black) and the asymmetric configuration (in red). The current density $\boldsymbol{J}$ is defined as

$$\boldsymbol{J} = \boldsymbol{\nabla} \times \boldsymbol{B}, \tag{4}$$

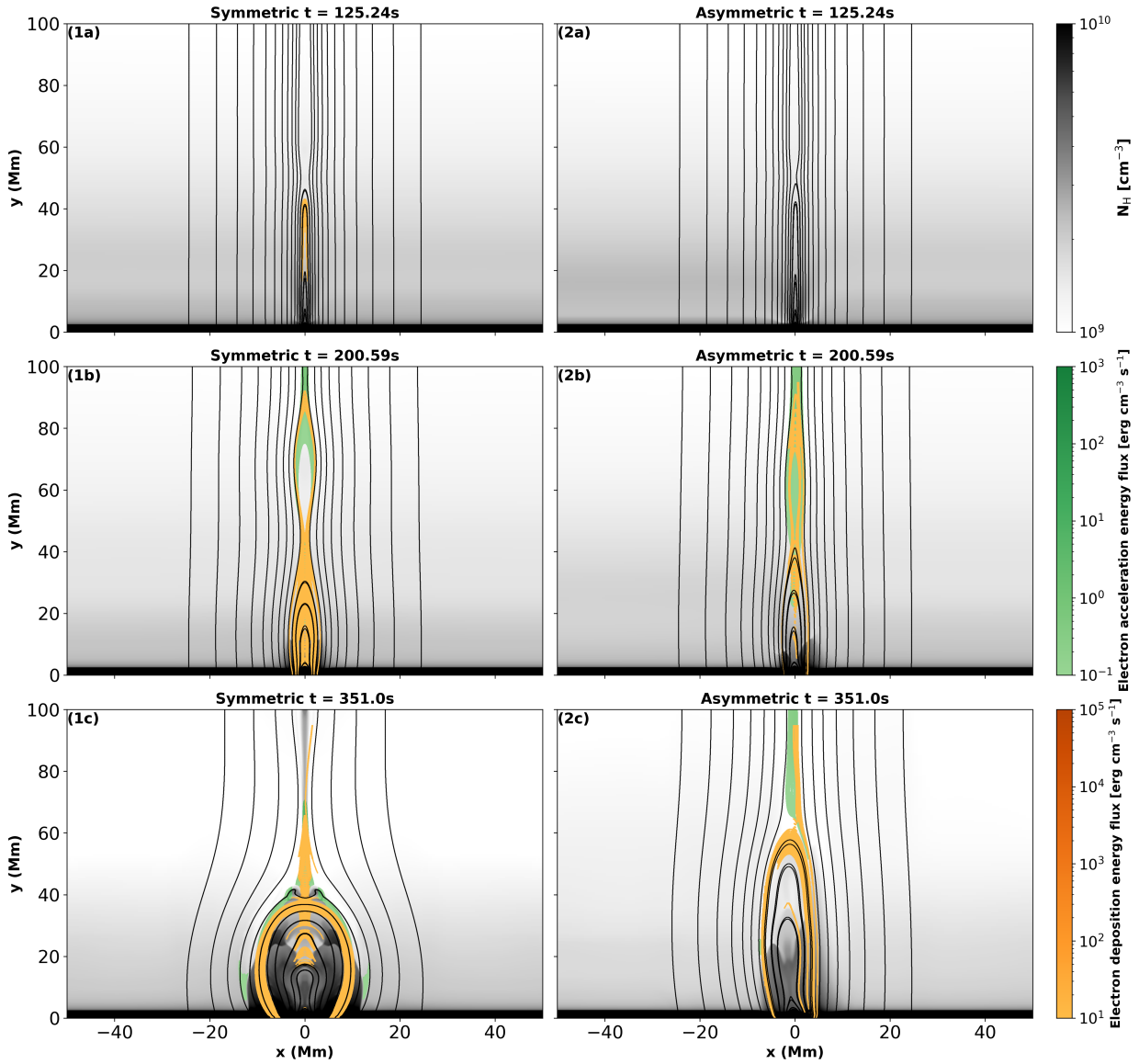


Figure 2. Snapshots of the symmetric (panels (1a), (1b), and (1c)) and asymmetric (panels (2a), (2b), and (2c)) simulations at $t = 125$ s, $t = 200$ s, and $t = 351$ s. All panels show the plasma density (gray color map) with overlays of electron deposition energy flux (in yellow-to-orange color map) and electron acceleration energy flux (in light-to-dark-green color map). Magnetic field lines are plotted in all panels with solid black lines.

such that initially (when $B_x = 0$ everywhere in the domain)

$$J_z(x) = \partial_x B_y(x). \tag{5}$$

Panel (d) of Figure 1 displays the $J_z(x)$ component of the current density for the two configurations mentioned previously. We can then ensure that the fields in our initial conditions are force-free, i.e.,

$$\boldsymbol{J} \times \boldsymbol{B} = 0. \tag{6}$$

In the cases presented, this leads to a general equation for B_z,

$$B_z(x) = \sqrt{k - B_y^2(x)}\,, \tag{7}$$

where k is a constant such that $B_z(x) \in \mathbb{R}$. Hence, the Cartesian force-free setup has a constant total magnetic field strength, but the vertical line-of-sight $B_z(x)$ varies strongly: this is the typical observed asymmetry across the polarity inversion at $x = 0$ that we model here. $B_z(x)$ for the two different configurations can be seen in panel (b) of Figure 1. Under the force-free fields condition, we also get

$$J_y(x) = J_z(x)\frac{B_y(x)}{B_z(x)}. \tag{8}$$

This is displayed in panel (c) of Figure 1.

Electrons are accelerated based on the criteria described by Equation (7) in M. Druett et al. (2024), on the apex of their corresponding magnetic field lines. For the field line analysis, coordinates and beam electron statistics were extracted directly from the tracked flare field lines (see W. Ruan et al. 2020). Other derived parameters are linearly interpolated from the values saved on the experiment grid outputs at the locations specified on the tracked field lines. We let the simulation run for a total of 1400 s. An animation of the simulation can be found as the interactive version of Figure 5.

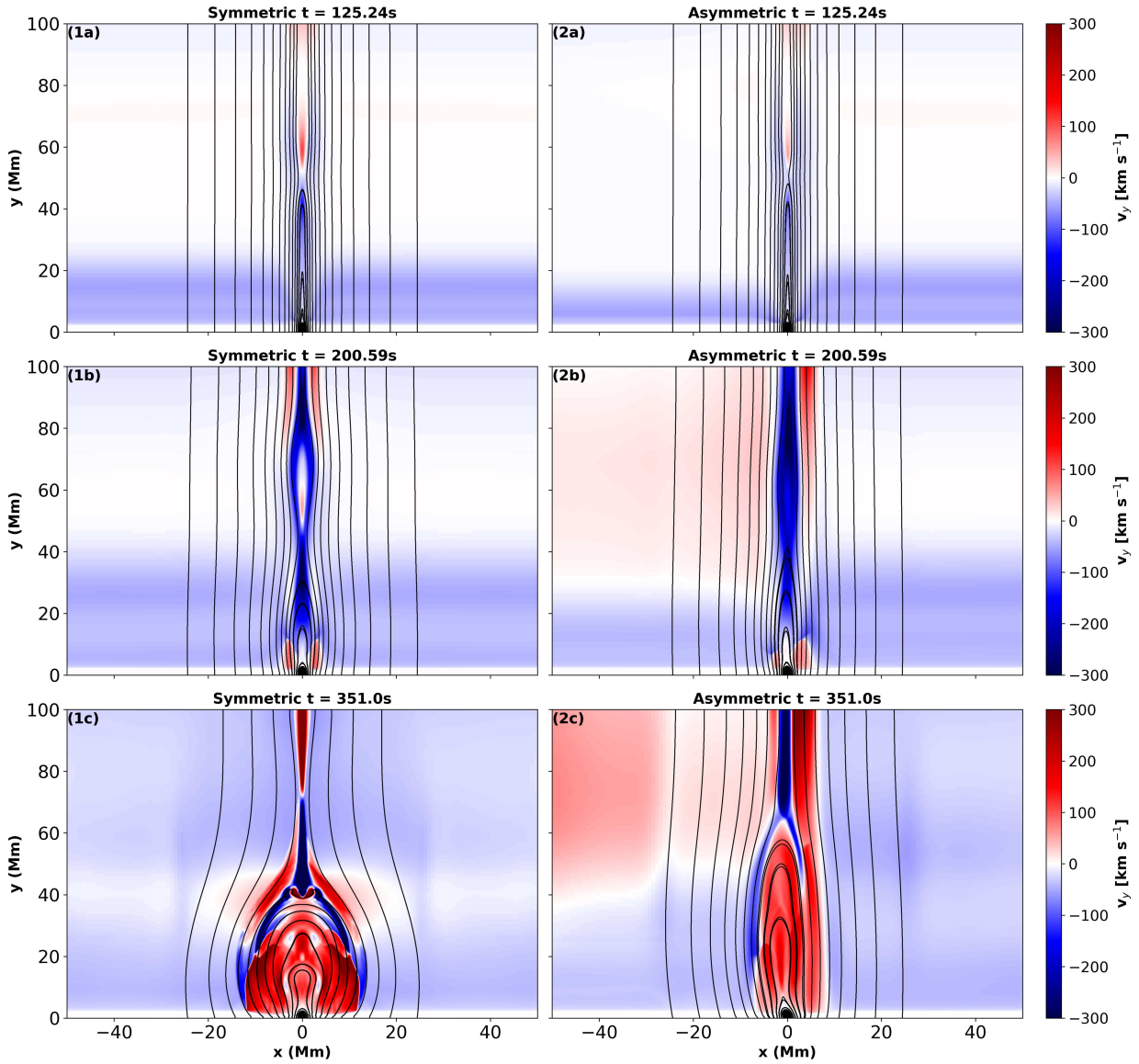


Figure 3. Snapshots of the symmetric (panels (1a), (1b), and (1c)) and asymmetric (panels (2a), (2b), and (2c)) simulations at $t = 125$ s, $t = 200$ s, and $t = 351$ s. All panels show the vertical velocity v_y. Magnetic field lines are plotted in all panels with solid black lines.

3. Results

Figure 2 shows a comparison between the symmetric and asymmetric configurations of the plasma density at three different times, $t = 125$ s, $t = 200$ s, and $t = 351$ s. Electrons are accelerated near sites of actively evolving reconnection and deposit their energy along the magnetic field lines to lower atmospheric regions. The electron acceleration flux is highlighted in green, while the electron deposition flux is highlighted in orange. Figure 3 shows a similar comparison for the y-component of the velocity, with the red color highlighting upward velocity and the blue color highlighting downward velocity.

The top panels of Figure 2 (panels (1a) and (2a)) display that while magnetic reconnection occurs in both configurations, electron acceleration is triggered at an earlier time in the case of the symmetric configuration, as highlighted in panel (1a) (and its absence in panel (2a)). The asymmetry of the configuration is also highlighted by a slightly bent magnetic field line around $Y = 50$ Mm in panels (2a) in both Figures 2 and 3, as well as lower ejection velocities above the reconnection point compared to the symmetric configuration (in red in panel (2a) of Figure 3).

After 200 s of simulation, the symmetric configuration still displays a reconnection point, as shown by the upward velocity around $Y = 50$ Mm in panel (1b) of Figure 3, while this point has disappeared in the asymmetric case. The asymmetric configuration presents a lobe-sided electron deposition flux, favoring the side $x > 0$ Mm, where the background magnetic field is stronger.

By 351 s of simulation, the reconnection X-point moved out of the simulation domain across the open top boundary for the asymmetric case, but it is still present in the symmetric case, as shown by the upward velocity above $Y = 50$ Mm in panel (1c) of Figure 3. Note that our top boundary treatment remains consistent with allowing reconnection downflows and associated electron acceleration sites. We do observe that the reconnection rate decreases in the asymmetric flare. Flare loops form in both simulations. The faster reconnection rate in the symmetric case is strongly evident through the faster separation of the flare footpoints and correspondingly wider

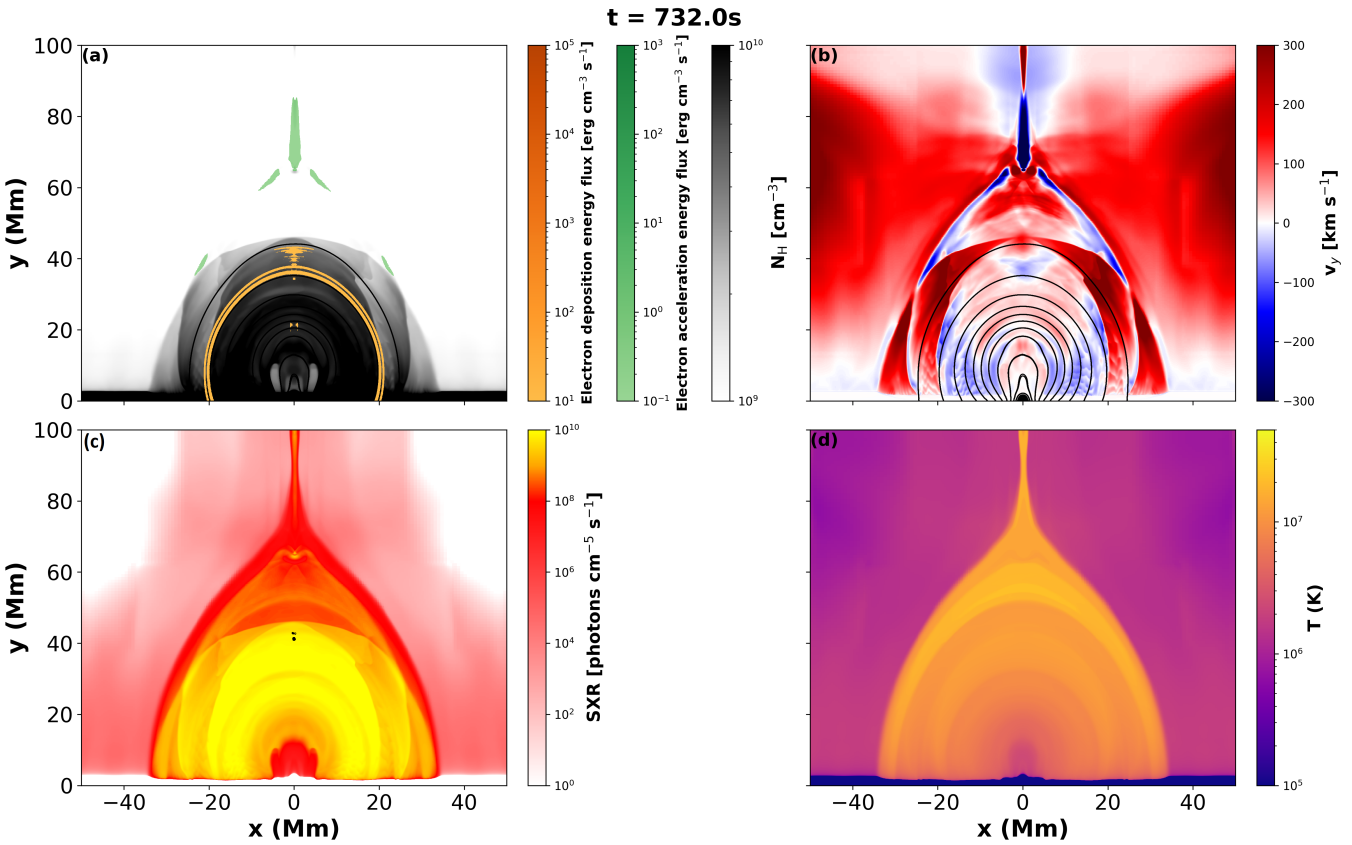


Figure 4. Snapshot at $t = 732$ s of (a) the plasma density (gray color map) with electron deposition energy flux (in yellow to orange color map) and electron acceleration energy flux (in light-to-dark-green color map); (b) the y-component of the plasma velocity; (c) the SXR color map, with HXR contours (black) at 0.1, 0.4, and 0.8 photons cm^{-5} s^{-1} (HXR is almost absent at this particular time); and (d) the temperature, for the symmetric configuration. Magnetic field lines are plotted with solid black lines.

flare loop system base present in the symmetric simulation (panel (1c) vs. panel (2c) of Figure 2). The wide footpoint half-separation of 14 Mm and lower loop-top system in the atmosphere, up to $Y \approx 40$ Mm, has resulted in stronger evaporation of chromospheric material, resulting in denser plasma within the loop tops, as shown by the darker coloring in panel (1c) of Figure 2. There is also deposition of energetic electron flux at the center of the loop tops. The asymmetric loop system is thinner and extends higher in the atmosphere, up to almost 60 Mm. The plasma density is lower within the flare loop, and energy deposition remains along the field lines that form the loop. The higher upward velocity within the loop in the symmetric configuration (panel (1c) of Figure 3) correlates with the higher plasma density. In the asymmetric case, a high upward velocity occurs outside of the flare loop, on the stronger background magnetic field side, ranging from the chromosphere up to the top of the simulation. This is not accompanied with a displacement of density (panel (2c) of Figure 2). This is likely slightly influenced by the top boundary, where the combination of gravitational stratification, dynamic magnetic field reconfigurations, and field-aligned thermal conduction is nontrivial to handle numerically.

3.1. Rotating Flux Rope

Figures 4 and 5 highlight a later stage, at $t = 732$ s, of the symmetric and asymmetric configurations, respectively. In both figures, panels (a) display a gray color map of the plasma density with electron deposition energy flux (in yellow-to-orange color map) and electron acceleration energy flux (in light-to-dark-green color map). Panels (b) display a color map of the vertical velocity; panels (c) display a color map of the SXR, with HXR contours highlighted in black; and panels (d) display a color map of the plasma temperature. The symmetric case at this time in Figure 4 shows quasi-periodic pulsations at its loop top, and the HXR emission reduces during this time, as discussed in Section 3.2. In the asymmetric configuration from Figure 5, a rotating flux rope is produced beneath the flaring loop system. This flux rope can be observed through the electron deposition flux located between $X = -5$ and $X = +5$ Mm (panel (a) of Figure 5). It is also visible through the shift between upward and downward velocity at the same location in panel (b) of Figure 5. This flux rope is magnetically connected to the chromosphere at about $x = 2$ Mm and is associated with an HXR footpoint source (panel (c)). From $t = 600$ s onward, an area of denser plasma forms at the top of the center of the loop (see panel (a) of the interactive version of Figure 5). This dense plasma, associated with higher SXR at the same location, precedes the appearance of the electron deposition flux associated with the rotating flux rope. The rotation of the plasma is likely due to pressure gradients and magnetic restructuring, influenced by Lorentz forces, induced by the asymmetry of the system within the flare loop. Both density and velocity values are in order-of-magnitude agreement with the rotating flux rope produced in V. Liakh & R. Keppens (2023). However, its temperature remains of the order of 10^7 K, never reaching cooler temperatures below the 10^6 K typically observed. Due to the absence of transition

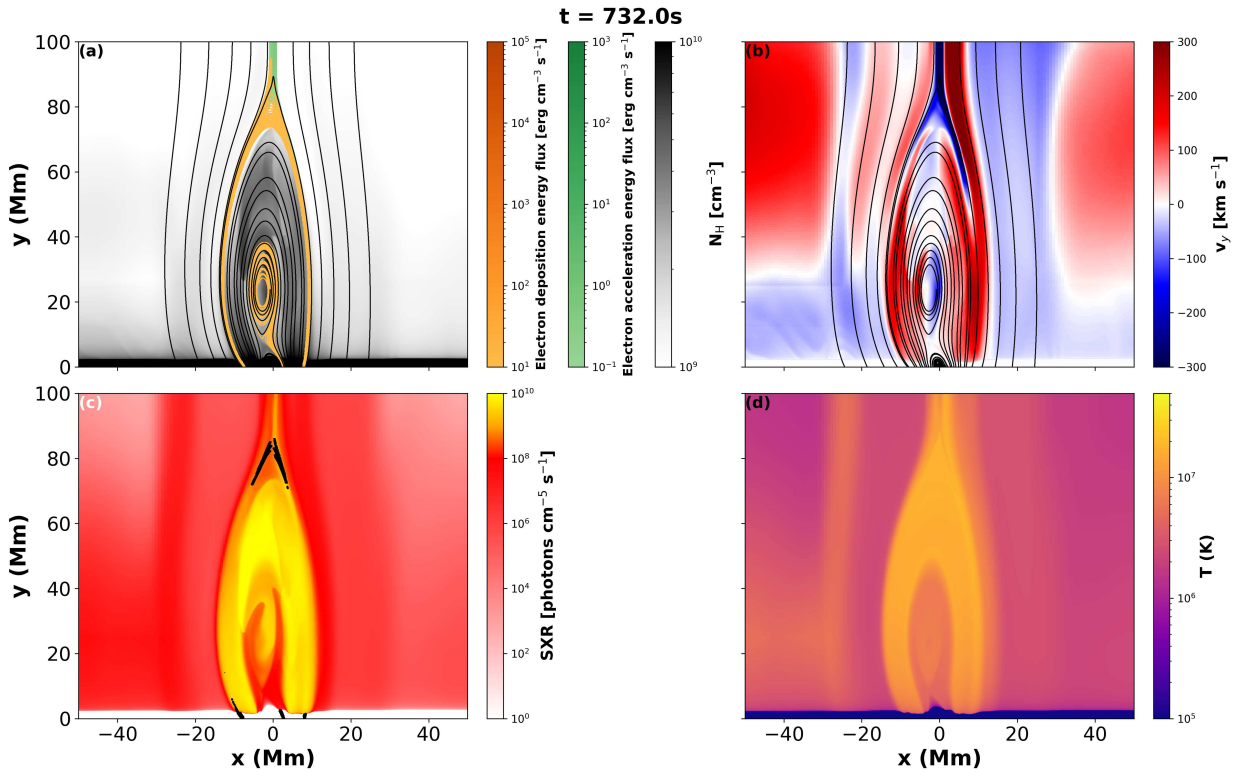


Figure 5. Snapshot at $t = 732$ s of (a) the plasma density (gray color map) with electron deposition energy flux (in yellow-to-orange color map) and electron acceleration energy flux (in light-to-dark-green color map); (b) the y-component of the plasma velocity; (c) the SXR color map, with HXR contours (black) at 0.1, 0.4, and 0.8 photons cm^{-5} s^{-1}; and (d) the temperature, for the asymmetric configuration. Magnetic field lines are plotted with solid black lines. An animation of the full simulation is also available by interacting with the figure. It shows the full length of the simulation, from $t = 0$ s to $t = 1400$ s. It includes the initial reconnection, electron beam transport, and flux rope formation.

(An animation of this figure is available in the online article.)

region adaptive conduction (TRAC; Y. Zhou et al. 2021), evaporation is underestimated, which leads to insufficient cooling to form coronal rain. This flux rope formation mechanism is absent in the symmetric configuration.

This rotating flaring flux rope structure is the first to appear in this suite of flare simulations. It adds another vortex generation scenario to the recent simulations that have generated rotating structures in prominences (V. Liakh & R. Keppens 2023; A. G. M. Pietrow et al. 2024b; V. Liakh & R. Keppens 2025), and, through the formation of a new flux rope, it could provide a basis to study flares and flare ribbons beneath double flux ropes, or double-decker filament systems (B. Kliem et al. 2014; X. M. Zhang et al. 2024). Future simulations should enlarge the vertical extent of our domain to simultaneously follow the fate of the assumed larger flux rope system that erupts above the original X-point.

3.2. Hard and Soft X-Ray Fluxes

SXR emission is estimated through thermal bremsstrahlung, while HXR emission is estimated through nonthermal bremsstrahlung (W. Ruan et al. 2020). Our beam treatment has all important information of the associated energy spectrum as it evolves along the reconnecting field lines, so we can provide HXR images, quantify the pitch-angle distribution associated with the beams, and identify sites of particle trapping. The beams themselves are fully aware of the column depths they encounter along their field-aligned trajectories and follow thick-target prescriptions.

In the symmetric configuration (Figure 4), the wide extent of the flare loop system allows wider deposition sites, about 2 Mm wide. The asymmetric configuration produces a thinner, more elongated loop, which leads to a much lower deposition along the field lines within the loop and only two much thinner HXR footpoints in the expanding edges of the flare ribbons in the dense lower atmosphere.

The wider, lower loop system in the symmetric configuration leads to more efficient evaporation of hot dense plasma, and thus the SXR flux within the loops is much higher than for the asymmetric configuration. The asymmetry in this simulation has reduced the evaporation densities and hence the SXR fluxes. It also results in lower temperatures within the flare loop tops, as highlighted in panels (d) of Figures 4 and 5. However, the direct cause may more fundamentally be the reduced reconnection rates associated with the asymmetric simulation and the greater heights of the loop system.

Evaporating material can be observed on the edges of the loop in the symmetric configuration (in red in panel (b) of Figure 4), while the plasma at the core of the loop is moving toward the lower atmosphere. In the asymmetric configuration, the majority of the plasma within the loop is evaporating upward (panel (b) of Figure 5).

The integrated SXR (black) and HXR (red) fluxes for both configurations are shown in Figure 6. The solid lines correspond to the symmetric configuration, while the dashed lines correspond to the asymmetric configuration. The SXR fluxes start to increase when electron acceleration is enabled, indicated by the first vertical blue line at $t = 100$ s. We disabled electron

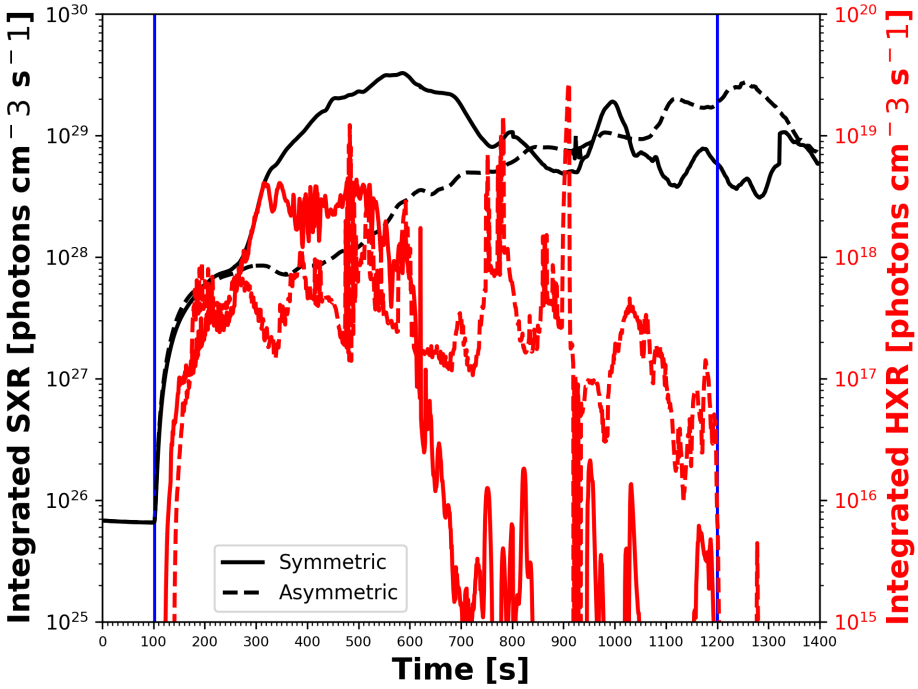


Figure 6. Time evolution of the spatially integrated (in X and Y) SXR (black) and HXR (red) fluxes during the simulation time. The solid lines show the fluxes for the symmetric configuration, while the dashed lines show the fluxes for the asymmetric configuration. The left and right blue vertical lines correspond to the time where electron acceleration is enabled and disabled, respectively, in the simulation.

acceleration at $t = 800$ s, indicated by the second vertical blue line at $t = 1200$ s. In the symmetric configuration (solid lines), the SXR flux departs from the one in the asymmetric configuration (dashed lines) around $t = 300$ s. As stated previously, the more efficient plasma evaporation in the wider loop of the symmetric configuration is correlated to higher SXR and HXR fluxes. Starting from $t = 600$ s, both SXR and HXR fluxes decrease, even while the electron acceleration is still enabled. After 380 s, the loop tops start to develop quasi-periodic oscillations as described in S. Takasao et al. (2015), S. Takasao & K. Shibata (2016), and M. Druett et al. (2024). These pulsations emit shocks into the loop, around every 16 s, which increases the density in the field lines that have recently reconnected (M. Druett et al. 2024). This increase in density removes energy from the electron beams before they can reach the lower atmosphere. The loop top acts as a thick target for the beams of electrons, similar to what is reported in W. Ruan et al. (2020). This reduction of the fluxes of electrons reaching the lower atmosphere directly reduces HXR emissions.

In the asymmetric configuration, however, the SXR and HXR fluxes are lower owing to the slower reconnection rate induced by the thinner, more elongated shape of the flare loop. This also leads to the absence of the previously mentioned periodic oscillations in the loop tops. The electron fluxes are not reduced as in the symmetric configuration, and HXR emissions remain present until the electron acceleration is turned off.

The time evolution of the location of the HXR footpoints in both configurations can be seen in Figure 7, with the symmetric configuration in panel (a) and the asymmetric configuration in panel (b). They are obtained by integrating the HXR fluxes in the lower dense atmosphere ($Y < 2.543$ Mm).

In the symmetric configuration, the footpoint location remains symmetrical as it expands outward. The intensity of the flux starts to decrease around 600 s, in agreement with Figure 6. Both the beam accelerated from the left ($X < 0$) and the beam accelerated from the right ($X > 0$) reach the dense lower atmosphere at the same time. In the expanding (outer) fronts of the flare ribbons, there are strong consistent signals from the onset of the beam (at around 180 s) up to around 380 s; the leading edge shows strong HXR signals, and only a very thin area ahead of this front shows the reduced fluxes that would be expected in light of the observations and simulations of V. Polito et al. (2023) and G. S. Kerr et al. (2024b). The acceleration criteria for electrons are also met in locations within the loop system, which produces broader, weaker bursts of HXR signals inside the main body of the flare ribbon.

In the case of the asymmetric configuration, the initial onset of the beams reaching the dense lower atmosphere occurs later than in the symmetric configuration. However, there is no measurable difference in the timing of the initial arrival of the beams in each footpoint, above what could only be attributed to thresholds of detection of HXR or atmospheric and spectral impacts. There is also no asymmetry in the location of the HXR footpoints when they first reach the lower atmosphere. The secondary onset occurring from 420 s does show a difference in onset time in opposite ends of the field loops. This relates to the asymmetry of the loop top and reconnection outflow conditions on either side of the reconnection point. This demonstrates that asymmetric coronal conditions in the outflows and the reconnection regions can potentially generate differing fluxes and onset times of beam energy delivery to the lower atmospheres, which is an additional consideration for interpretation of the timings of signals made in P. J. A. Simões et al. (2024).

The footpoint HXR flux is stronger on the side of stronger background magnetic field ($X > 0$) from the beam onset until around 400 s. This is the opposite relationship to that noted by T. Sakao (1994) and T. Sakao et al. (1996), i.e., a non-Sakao or N-type relationship. Although our model allows for magnetic

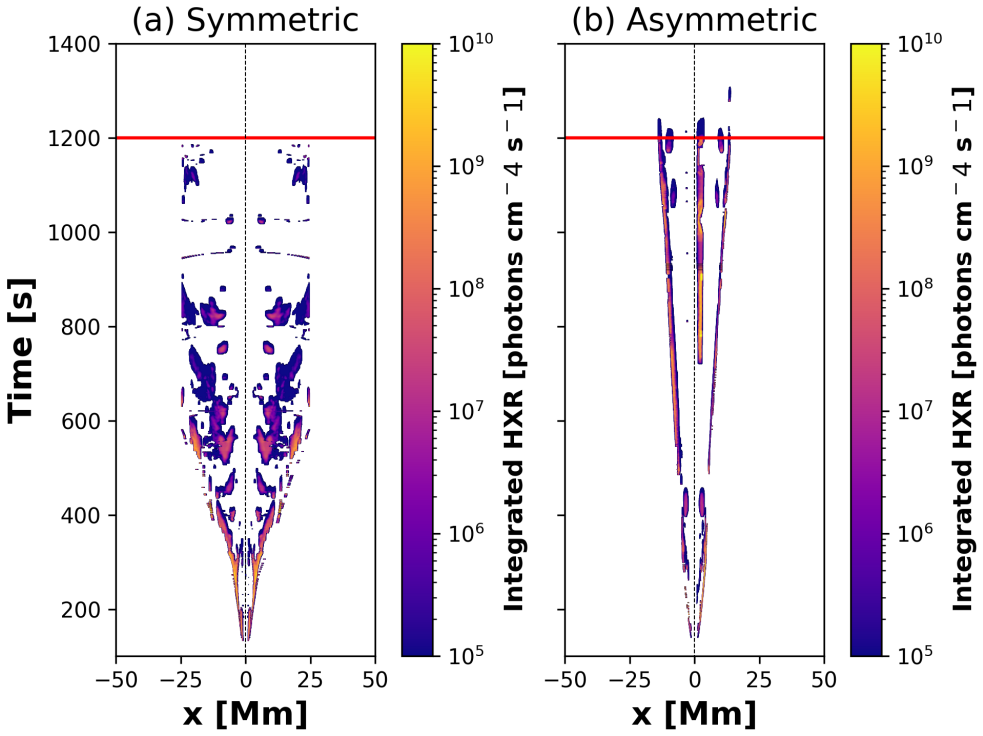


Figure 7. Time evolution of the location of the HXR footpoints (below the transition region, $Y < 2.543$ Mm) for (a) the symmetric configuration and (b) the asymmetric configuration. The red line highlights when the electron acceleration is disabled.

mirroring, the magnetic field strength at the bases of our models is much lower than those of a typical active region. This could explain why the mirroring has not been particularly effective. We also note that the initial pitch angle introduced in the simulation is $\theta = 18°$. W. Ruan et al. (2024) showed that higher initial pitch angle results in a higher particle trapping. Future investigations could investigate the influence of higher initial pitch angle on the non-Sakao relationship at the footpoints. At this point in our models it appears that the convergence of the field into tighter footpoints is potentially responsible for more intense footpoint fluxes on the side with greater field strength.

The footpoint attached to the rotating flux rope presented in the previous section can be seen to appear around 700 s in panel (b), displayed by the integrated HXR flux close to the $X = 0$ Mm line. Focusing on only the expanding ribbon front sources, from 500 s, we see a much broader, stronger source on the side with the weaker field strength ($X < 0$), which replicates the Sakao effect for the majority of the experiment time. Interestingly, even within the same two footpoint sources, we note the Sakao effect and non-Sakao effect in the same simulation. However, in this simulation, it appears that source and atmospheric asymmetry is a more likely candidate for both types of signal rather than magnetic mirroring.

Figure 8 displays the time evolution of the upward mass flux $\rho_H v_y$ in black and the upward velocity flow v_y in red in the asymmetric simulation. Each value is computed as an average over an area where SXR $>10^9$ photons cm^{-5} s^{-1}, which corresponds to the two feet of the flare loop at any point in time of the simulation. The footpoint located on the side with the stronger initial vertical magnetic field ($X > 0$) is shown with a dashed line, while the footpoint located on the side with the weaker initial vertical magnetic field ($X < 0$) is shown with a solid line. We observe that the side with the stronger initial magnetic field presents a strong upward mass flux and velocity from the start of the simulation until about $t = 800$ s. This correlates with our prior observation of the anti-Sakao effect on the same side. After this, both mass flux and upward velocity increase on the side with the weaker initial magnetic field and are briefly superior to their counterpart on the side with stronger magnetic field. This again correlates with the change of behavior of the HXR flux observed in Figure 7 and the appearance of the Sakao effect on this side.

3.3. Asymmetry and Field Line Analysis

Figure 9 displays the time evolution of the plasma density (panels (a) and (b)), the y-component of the velocity (panels (c) and (d)), and the plasma temperature (panels (e) and (f)) for the asymmetric configuration between $t = 101$ s and $t = 200$ s. The variables are interpolated along a field line traced starting at the location where the electron beams hit the lower atmosphere at $t = 141$ s, $X = -1.12$ Mm on the side where $\boldsymbol{B}_0 = 35$ G and $X = 1.15$ Mm on the side where $\boldsymbol{B}_0 = 50$ G. This field line is labeled "Onset."

Figure 10 displays the time evolution of the plasma density (panels (a) and (b)), the y-component of the velocity (panels (c) and (d)), and the plasma temperature (panels (e) and (f)) for the asymmetric configuration between $t = 300$ s and $t = 800$ s. The variables are interpolated along a field line traced from the location where the electron beams hit the lower atmosphere at $t = 600$ s, $X = -6.15$ Mm on the side where $\boldsymbol{B}_0 = 35$ G and $X = 6.18$ Mm on the side where $\boldsymbol{B}_0 = 50$ G. This field line is labeled "Body." In both Figures 9 and 10, a green dotted line marks the location of the transition region at $Y = 2.543$ Mm.

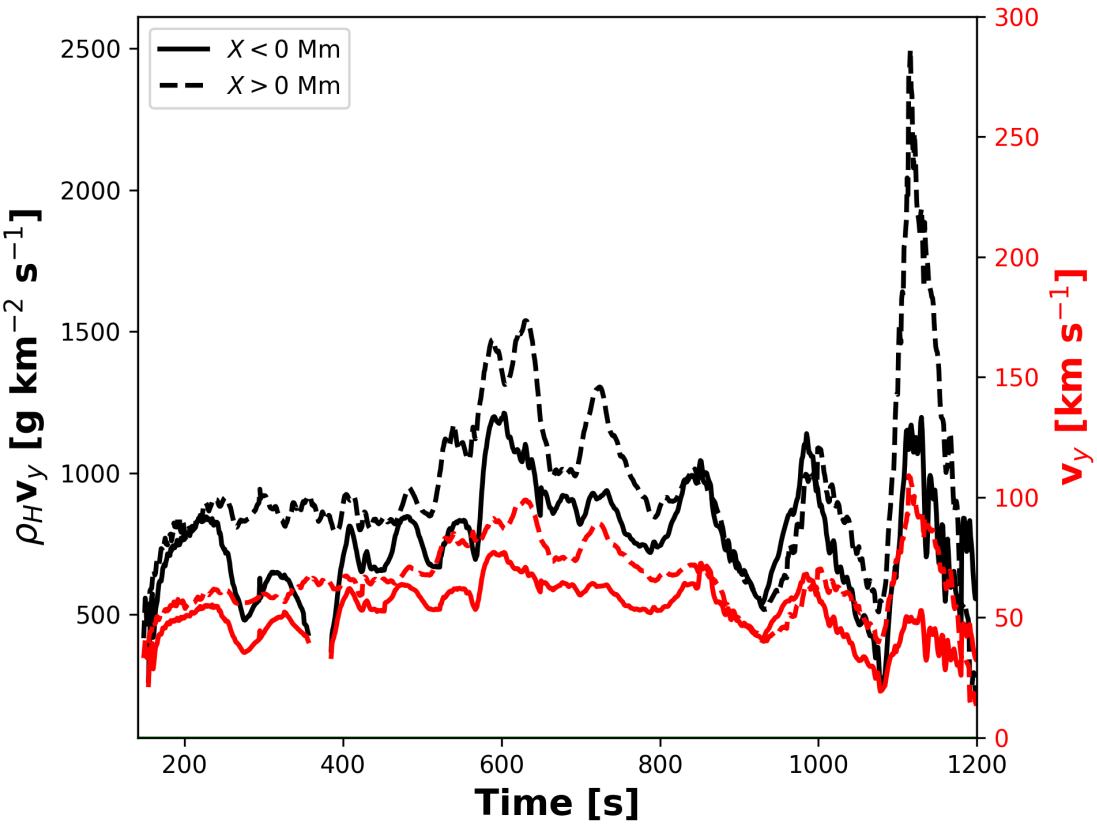


Figure 8. Time evolution of the upward mass flux $\rho_H v_y$ (black) and the upward velocity v_y (red) for the side with the stronger initial vertical magnetic field ($X > 0$; dashed line) and the side with the weaker initial vertical magnetic field ($X < 0$; solid line), in the asymmetric configuration.

3.3.1. Timing of Variables Transport

As stated previously, there is no difference in the timing of the arrival of the beams in the footpoints of the Onset line, as highlighted mostly by the upward velocity in the y-direction in panels (c) and (d) of Figure 9. Both beams interact with the dense lower atmosphere at the same time $t = 141$ s. In the case of the Body field line (panels (c) and (d) of Figure 10), all variables display an asymmetric behavior in timing. The side with $\boldsymbol{B}_0 = 35$ G presents a lower coronal density, temperature, and downward velocity before $t \approx 370$ s, contrary to the side with the stronger background magnetic field. This is due to the field line located outside of the flare loop, while the side with the stronger background magnetic field is experiencing the strong evaporation jet on the edge of the loop, already observed in panel (b) of Figure 5 at around $X = 7$ Mm. The presence of asymmetry later in the simulation, as well as its absence in the early stage, can again be explained with a possible weak asymmetry in the magnetic field. The flare loop takes around 300 s to exhibit true asymmetric behavior.

3.3.2. Chromospheric Evaporation

While the Onset line does not exhibit asymmetry in the timing of the beam in the early stage of the simulation, it does present an asymmetry in the evaporation flow of density, upward velocity, and temperature. After the beams have reached the lower atmosphere, density, upward velocity, and temperature in the corona are higher on the side of weaker background magnetic field, as highlighted in panels (a), (c), and (e) of Figure 9. The strong evaporation flow located on the edge of the flare loop on the side with $\boldsymbol{B}_0 = 50$ G, observed in the animated version of panel (b) of Figure 5, is possibly responsible for the weaker evaporation along the field line directly above the HXR footpoint. In contrast, the Body field line displays a stronger evaporation in density, upward velocity, and temperature directly above the HXR footpoint at $t = 600$ s on the side with $\boldsymbol{B}_0 = 50$ G, as can be seen in panels (b), (d), and (f) of Figure 10. This stronger evaporation is also accompanied by a deeper penetration in the lower atmosphere, as can be seen in panels (d) and (f), around $t = 600$ s.

4. Discussion and Conclusions

In this study, we adapted the model presented in W. Ruan et al. (2020) and M. K. Druett et al. (2023, 2024) to simulate beam-driven chromospheric evaporation in flare loops, and we directly confront the standard symmetric with an asymmetric magnetic configuration. Figures 7 and 9 show that, despite the asymmetry in the initial magnetic field, there is no asymmetry in the arrival time of the electron beams at the lower boundary. The initial formation of the flare loop after the first reconnection process remains fairly symmetrical, which leads to a symmetrical transport of the beams. The more pronounced asymmetric shape of the loop later in the simulation (i.e., $\approx$400 s; see Figure 10), which here leads to an asymmetric topology of the beams in the lower atmosphere, indicates that further studies with a stronger asymmetry of the initial magnetic field would be required to study a possible timing asymmetry in the arrival of the electron beams. The width of the current sheet (w in Equation (2)) may also play a role in the initial formation of the flare loop, with wider current sheet

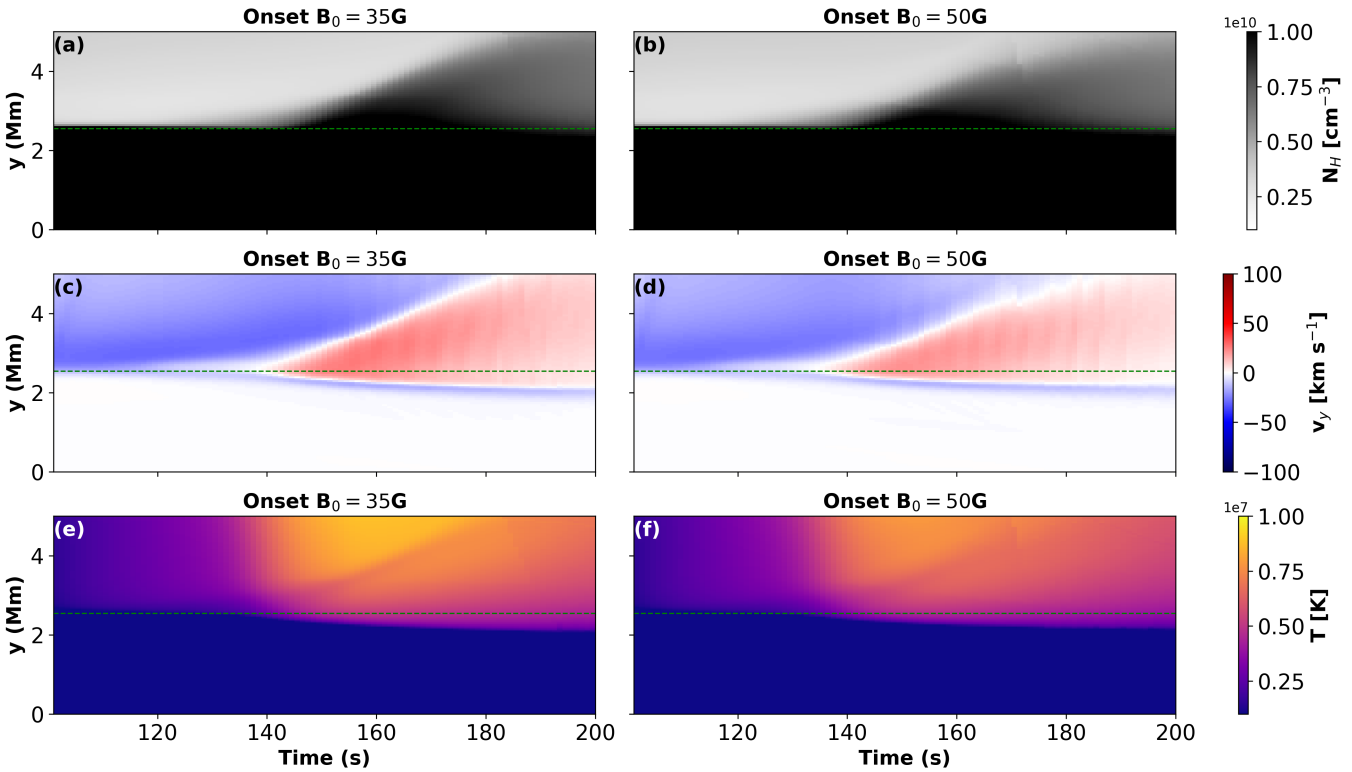


Figure 9. Time evolution of plasma density (panels (a) and (b)), v_y (panels (c) and (d)), and temperature (panels (e) and (f)) for the asymmetric configuration between $t = 101$ s and $t = 200$ s. Data are interpolated along a field line with a footpoint located at $X = -1.12$ Mm on the side where $\boldsymbol{B}_0 = 35$ G and $X = 1.15$ Mm on the side where $\boldsymbol{B}_0 = 50$ G at $t = 141$ s, labeled "Onset." The green dotted line at $Y = 2.543$ Mm marks the location of the transition region.

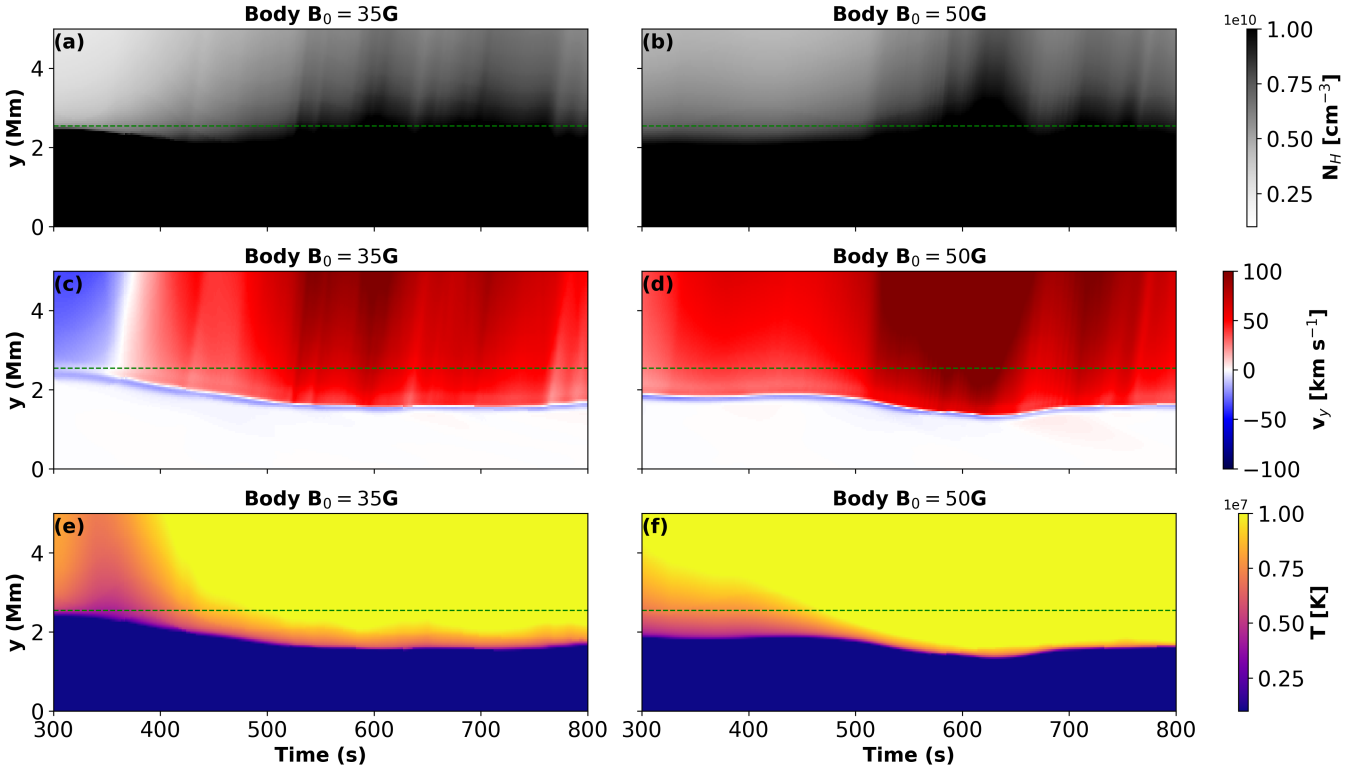


Figure 10. Time evolution of plasma density (panels (a) and (b)), v_y (panels (c) and (d)), and temperature (panels (e) and (f)) for the asymmetric configuration between $t = 300$ s and $t = 800$ s. Data are interpolated along a field line with footpoint located at $X = -6.15$ Mm on the side where $\boldsymbol{B}_0 = 35$ G and $X = 6.18$ Mm on the side where $\boldsymbol{B}_0 = 50$ G at $t = 600$ s, labeled "Body." The green dotted line at $Y = 2.543$ Mm marks the location of the transition region.

increasing the initial asymmetry in the system. However, this also increases the time at which reconnection first occurs, increasing the duration of the simulation. P. J. A. Simões et al. (2024) observe a difference in timing in footpoint sources between 0.14 and 0.42 s, which is below the output cadence of this simulation. Time-dependent beam particle transport should be included in the model before an assessment of the relative impacts of these approaches is concluded. This is left for future investigations. P. J. A. Simões et al. (2024) also note that the pitch-angle distribution of electrons in the loop top may influence the transport of said electrons along the magnetic field line, i.e., trapped particles may introduce a delay in the transport. W. Ruan et al. (2020) highlighted that higher initial pitch angle in the loop top increases HXR emission. Statistical studies with varying pitch-angle distribution would also provide valuable insight on the timing of transport of the electron beams. These aspects are left for future follow-up studies.

After a significant time has passed in the simulation ($t > 700$ s), the asymmetric configuration leads to the formation of a rotating plasma flow in the center of the flare loop, as indicated in panel (b) of Figure 5. This flow is accompanied by a circular electron deposition flux (panel (a) of Figure 5), indicating the presence of a rotating flux rope. This flux rope is magnetically attached to the dense lower atmosphere and produces an HXR footpoint. It is also associated with an increase in plasma density, as also observed by V. Liakh & R. Keppens (2023), and a rise in SXR emission. However, contrary to the rotating structure shown by V. Liakh & R. Keppens (2023), the rotating flow in this simulation is not associated with a decrease in temperature. The currently adopted, simplified description of the transition region, presented in W. Ruan et al. (2020), underestimates the evaporation in the simulation and hinders the formation of potential coronal rain, which was, however, demonstrated recently in a 3D flare setup by W. Ruan et al. (2024) when using a TRAC algorithm. This is a well-known shortcoming of underresolved transition region physics, which inspired the development of tailor-made modifications that remedy this by a suitable adaptation of both the local radiative losses and the local heat flux (C. D. Johnston & S. J. Bradshaw 2019). We plan to revisit these models using the multidimensional TRAC variant (Y. Zhou et al. 2021) that will lead to a more realistic evaporation scheme for the study of flare-associated coronal rain in 2.5D simulation with electron beams. We also note that this flux rope is not rising and erupting in our simulation and is to be differentiated from the (as-yet-unmodeled) actually erupting flux rope system that ejects above the initial X-point. It will be of interest to investigate the same setups in domains with a larger vertical extent, to capture the fate of the flux rope we now find forming in the asymmetric flare loop system, along with the flux rope that should be erupting above the domain simulated here, as depicted in the standard flare model. This may well lead to significant differences in the overall evolution and is best addressed in full 3D settings, clarifying the topology and the (line-tied) footpoints of either flux rope structure.

The integrated SXR and HXR fluxes in the asymmetric configuration are sustained throughout the duration of the simulation, as highlighted in Figure 6. The magnetic fork tuning effect, observable in the symmetric configuration of M. K. Druett et al. (2023, 2024), appears much later (around $t = 800$ s) in the case of the asymmetric configuration, due to the lowest reconnection rate induced by the thinner, more elongated shape of the flare loop.

Figure 7 highlights a non-Sakao relationship (T. Sakao 1994; T. Sakao et al. 1996), i.e., a stronger footpoint HXR flux on the side with the stronger background magnetic field ($X > 0$), from the beam onset until around 400 s. From $t = 500$ s onward, we see a stronger source of HXR flux on the side with the weaker background magnetic field ($X < 0$). This replicates the Sakao effect. There are two important notes to make here. The first point is that, despite having the same electron energy input that leads to HXR footpoints on both sides, we see both the Sakao and non-Sakao effects. The reversal could be explained by a strong evaporation upward flow on the side with the weaker background magnetic field after $t = 500$ s (see the interactive version of Figures 5 and 8). It was not present until this point, due to the asymmetry of the flare loop. It is also consistent with the observations of G. S. Kerr et al. (2026), with the weaker HXR footpoint being driven mainly by thermal heat flux, while the stronger HXR footpoint was mainly driven by electron precipitation. The second note is that, despite observing both effects, it is unlikely that it is due to the mirroring of electron beams in our simulation. The magnetic field strength at the footpoint of our magnetic field lines is much lower than what is typically observed in a solar active region.

Figures 9 and 10 confirm that, despite the asymmetric configuration, there is no asymmetry in the timing of the beams at the lower atmosphere. We note that the distance between the absolute value coordinates of both field lines' footpoints displayed in Figures 9 and 10 is about 30 km. Although there appears to be an asymmetry in the location of their footpoints, this distance is smaller than the finest resolution of our simulations, i.e., $\Delta X = 48.8$ km. We thus assume that there is no asymmetry here. However, we observe an asymmetry in the evaporation scheme, with the side of weaker background magnetic field presenting stronger evaporation flows at early stages of the simulation. This behavior then switches, with the side with the stronger background magnetic field displaying stronger evaporation flows. This switch follows the switch from the non-Sakao effect to the Sakao effect observed previously. We thus observe that the non-Sakao effect is associated with weaker evaporation flows, while the Sakao effect is associated with stronger evaporation flows.

This study presents the first multidimensional magneto-hydrodynamic flare simulation featuring evaporation driven by energetic electron beams that have an asymmetric magnetic field configuration. We evidenced that this configuration leads to a vastly different shape of the flare loop compared to the symmetric configuration, including the formation of a rotating flux rope, and exhibits both the anti-Sakao and Sakao effects in the same simulation.

We note that a number of improvements could be beneficial to this study. Multiple parametric studies can be conducted to study the influence of various parameters on the simulation. Several preliminary tests suggest that the width of the current sheet, the height of the reconnection X-point (initially located at $Y = 50$ Mm in this simulation), and the initial magnetic field asymmetry all influence the reconnection rate of the simulation. These parameters may also play a role in the timing and propagation of the electron beams. Variations in the height

might influence the shape of the flare loop, as well as the beam parameters. These parameters may also influence the beam pitch-angle distribution. A study of the evolution of such parameters could provide key insights on the reversal of the Sakao effect throughout the simulation, in addition to the already-observed asymmetric loop geometry. Our finite extent in height and the associated need to handle a complex top open boundary behavior numerically are also aspects that we need to improve in further work, since the asymmetric run has its initial X-point crossing this boundary.

Another aspect that can be varied relates to the electron beam modeling for a more accurate and quantitative comparison with observations. The current model only accelerated electrons at the apex of each field line. Acceleration at physically identified, appropriate locations along each field line would be required further on. Additional improvements could be made by adding the contribution of those beams toward the momentum equation describing the simulation, as well as adding possible return currents. Methods beyond the thick-target model should be envisaged. We note that the role played by MHD wave transport (A. J. B. Russell & D. J. Stackhouse 2013), in our multidimensional settings, is actually incorporated fully, as that forms part of the thermal evolution governed by the MHD description.

Extending this model toward three dimensions would be a step further toward global flare modeling. 3D, asymmetric simulations could be used to study the formation mechanisms of quasi-periodic pulsations, which can be observed during large solar flares (L. A. Hayes et al. 2019) and whose formation mechanisms are still vastly debated (I. V. Zimovets et al. 2021). The formation of a rotating flux rope would have to be studied in this third dimension, as well as the influence of the beams and their propagation on the formation of post-flare rain condensations (W. Ruan et al. 2024). Finally, the entire 3D flux rope ejection, appearing above the reconnection X-point, is not described in this simulation.

Acknowledgments

The computational resources and services used in this work were provided by the VSC (Flemish Supercomputer Center), funded by the Research Foundation Flanders (FWO) and the Flemish Government, department EWI. M.D. and R.K. acknowledge funding from the KU Leuven C1 project C16/24/010 UnderRadioSun and the Research Foundation Flanders FWO project G0B9923N Helioskill.

ORCID iDs

M. Dubart https://orcid.org/0000-0002-1655-4601
M. Druett https://orcid.org/0000-0001-9845-266X
W. Ruan https://orcid.org/0000-0001-5045-827X
R. Keppens https://orcid.org/0000-0003-3544-2733

References

Allred, J. C., Kowalski, A. F., & Carlsson, M. 2015, ApJ, 809, 104
Bacchini, F., Ruan, W., & Keppens, R. 2024, MNRAS, 529, 2399
Čada, M., & Torrilhon, M. 2009, JCoPh, 228, 4118
Carlsson, M., Fletcher, L., Allred, J., et al. 2023, A&A, 673, A150
Chen, P. F., Fang, C., Tang, Y. H., & Ding, M. D. 1999, ApJ, 513, 516
Colgan, J., Abdallah, J., Jr., Sherrill, M. E., et al. 2008, ApJ, 689, 585
De Pontieu, B., Title, A. M., Lemen, J. R., et al. 2014, SoPh, 289, 2733
Druett, M., Ruan, W., & Keppens, R. 2024, A&A, 684, A171
Druett, M., Scullion, E., Zharkova, V., et al. 2017, NatCo, 8, 15905
Druett, M. K., Ruan, W., & Keppens, R. 2023, SoPh, 298, 134
Falewicz, R., & Siarkowski, M. 2007, A&A, 461, 285
French, R. J., Kazachenko, M. D., Berghmans, D., et al. 2025, ApJL, 995, L54
Goff, C. P., Matthews, S. A., van Driel-Gesztelyi, L., & Harra, L. K. 2004, A&A, 423, 363
Harten, A., Lax, P. D., & Leer, B. 1983, SIAMR, 25, 35
Hayes, L. A., Gallagher, P. T., Dennis, B. R., et al. 2019, ApJ, 875, 33
Hurford, G. J., Schmahl, E. J., Schwartz, R. A., et al. 2002, SoPh, 210, 61
Izquierdo-Guzmán, I., González-Avilés, J. J., & Guzmán, F. S. 2023, SoPh, 298, 109
Jin, M., & Ding, M. D. 2007, A&A, 471, 705
Johnston, C. D., & Bradshaw, S. J. 2019, ApJL, 873, L22
Keppens, R., Meliani, Z., van Marle, A. J., et al. 2012, JCoPh, 231, 718
Keppens, R., Popescu Braileanu, B., Zhou, Y., et al. 2023, A&A, 673, A66
Keppens, R., Zhou, Y., & Xia, C. 2025, LRSP, 22, 4
Kerr, G. S., Kowalski, A. F., Allred, J. C., Daw, A. N., & Kane, M. R. 2024a, MNRAS, 527, 2523
Kerr, G. S., Krucker, S., Allred, J. C., et al. 2026, NatAs,
Kerr, G. S., Polito, V., Xu, Y., & Allred, J. C. 2024b, ApJ, 970, 21
Kliem, B., Török, T., Titov, V. S., et al. 2014, ApJ, 792, 107
Kong, X., Guo, F., Shen, C., et al. 2019, ApJL, 887, L37
Kowalski, A. F., Allred, J. C., Carlsson, M., et al. 2022, ApJ, 928, 190
Kowalski, A. F., Hawley, S. L., Carlsson, M., et al. 2015, SoPh, 290, 3487
Kumar, S., Nakariakov, V. M., & Moon, Y.-J. 2016, ApJ, 824, 8
Liakh, V., & Keppens, R. 2023, ApJL, 953, L13
Liakh, V., & Keppens, R. 2025, A&A, 696, A158
Mora, C., Bacchini, F., & Keppens, R. 2026, A&A, 706, A32
Mulay, S. M., & Fletcher, L. 2021, MNRAS, 504, 2842
Mulay, S. M., Fletcher, L., Hudson, H., & Labrosse, N. 2023, MNRAS, 526, 4755
Müller, D., St. Cyr, O. C., Zouganelis, I., et al. 2020, A&A, 642, A1
Nakariakov, V. M., Afanasyev, A. N., Kumar, S., & Moon, Y.-J. 2017, ApJ, 849, 62
Osborne, C. M. J., & Fletcher, L. 2022, MNRAS, 516, 6066
Pietrow, A. G. M., Druett, M. K., & Singh, V. 2024a, A&A, 685, A137
Pietrow, A. G. M., Liakh, V., Osborne, C. M. J., Jenkins, J., & Keppens, R. 2024b, A&A, 690, L15
Polito, V., Kerr, G. S., Xu, Y., Sadykov, V. M., & Lorincik, J. 2023, ApJ, 944, 104
Porth, O., Xia, C., Hendrix, T., Moschou, S. P., & Keppens, R. 2014, ApJS, 214, 4
Rimmele, T. R., Warner, M., Keil, S. L., et al. 2020, SoPh, 295, 172
Ruan, W., Keppens, R., Yan, L., & Antolin, P. 2024, ApJ, 967, 82
Ruan, W., Xia, C., & Keppens, R. 2020, ApJ, 896, 97
Ruan, W., Yan, L., & Keppens, R. 2023, ApJ, 947, 67
Russell, A. J. B., & Stackhouse, D. J. 2013, A&A, 558, A76
Saint-Hilaire, P., Krucker, S., & Lin, R. P. 2008, SoPh, 250, 53
Sakao, T. 1994, PhD thesis, The University of Tokyo
Sakao, T., Kosugi, T., Masuda, S., et al. 1996, AdSpR, 17, 67
Shen, C., Chen, B., Reeves, K. K., et al. 2022, NatAs, 6, 317
Simões, P. J. A., Fletcher, L., Hudson, H. S., et al. 2024, MNRAS, 532, 705
Singh, V., Scullion, E., Botha, G. J. J., et al. 2026, ApJ, 1007, 99
SPICE Consortium, Anderson, M., Appourchaux, T., et al. 2020, A&A, 642, A14
Takasao, S., Matsumoto, T., Nakamura, N., & Shibata, K. 2015, ApJ, 805, 135
Takasao, S., & Shibata, K. 2016, ApJ, 823, 150
Thoen Faber, J., Joshi, R., Rouppe van der Voort, L., et al. 2026, A&A, 705, A174
van Leer, B. 1974, JCoPh, 14, 361
Vernazza, J. E., Avrett, E. H., & Loeser, R. 1981, ApJS, 45, 635
Wu, H., Guo, Y., Keppens, R., et al. 2025, ApJ, 992, 81
Xia, C., Teunissen, J., Mellah, I. E., Chané, E., & Keppens, R. 2018, ApJS, 234, 30
Zhang, X. M., Guo, J. H., Guo, Y., Ding, M. D., & Keppens, R. 2024, ApJ, 961, 145
Zhou, Y., Ruan, W., Xia, C., & Keppens, R. 2021, A&A, 648, A29
Zimovets, I. V., McLaughlin, J. A., Srivastava, A. K., et al. 2021, SSRv, 217, 66